Journal of Materials Chemistry A

Accepted Manuscript

ROYAL SOCIETY OF CHEMISTRY

www.rsc.org/materialsA

Inverted All-polymer Solar Cells Based on a Quinoxaline-thiophene/Naphthalene-imide Polymer Blend Improved by Annealing

*Yuxin Xia, Chiara Musumeci, Jonas Bergqvist, Wei Ma, Feng Gao, Zheng Tang, Sai Bai, Yizheng Jin, Chenhui Zhu, Renee Kroon, Cheng Wang, Mats R. Andersson, Lintao Hou, Olle Inganäs *and Ergang Wang **

Thermal annealing on TQ1: N2200 polymer-polymer solar cells achieves higher J_{sc} and *FF*, and finally almost doubled PCE.

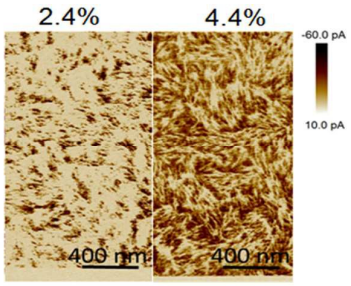

Figure 1. Current maps as-spun (left) and annealed (right) blend films. The current maps are measured under a -2 V bias applied to the ITO/ZnO substrate. In the maps darker colors correspond to higher current values. The numbers on top are the corresponding maximum PCEs of the inverted solar cells.

Journal of

Materials Chemistry A

ARTICLE

Inverted All-Polymer Solar Cells Based on a Quinoxaline-Thiophene/ Naphthalene-Imide Polymer Blend Improved by Annealing

Received 00th January 20xx,
Accepted 00th January 20xx

DOI: 10.1039/x0xx00000x

www.rsc.org/

Yuxin Xia,[a,f] *Chiara Musumeci,*[a] *Jonas Bergqvist,*[a] *Wei Ma,*[b] *Feng Gao,*[a] *Zheng Tang,*[a] *Sai Bai,*[a] *Yizheng Jin,*[c] *Chenhui Zhu,*[d] *Renee Kroon,*[e] *Cheng Wang,*[d] *Mats R. Andersson,*[e] *Lintao Hou,*[f] *Olle Inganäs** [a] *and Ergang Wang**[g]

We have investigated the effect of thermal annealing on the photovoltaic parameters of all-polymer solar cells based on a quinoxaline-thiophene donor polymer (TQ1) and an naphthalene diimide acceptor polymer (N2200). Annealed devices show doubling power conversion efficiency compared to non-annealed devices, due to higher short-circuit current (J_{sc}) and fill factor (*FF*), but with a lower open circuit voltage (V_{oc}). On the basis of the morphology—mobility examination by several scanning force microscopy techniques, and by grazing-incidence wide-angle x-ray scattering, we conclude that the better charge transport is achieved by higher order and better interconnected networks of the bulk heterojunction in the annealed active layers. The annealing improves charge transport and extends the conjugation length of the polymers, which do help charge generation and meanwhile reduce recombination. Photoluminescence, electroluminescence, and light intensity dependence measurements reveal how this morphological change affects charge generation and recombination. As a result, the J_{sc} and *FF* are significantly improved. However, the smaller band gap and the higher HOMO level of TQ1 upon annealing causes a lower V_{oc}. The blend of an amorphous polymer TQ1, and a semi-crystalline polymer N2200, can thus be modified by thermal annealing to double the power conversion efficiency.

1. Introduction

Polymer solar cells (PSCs) have been widely studied as a potential source of renewable electricity and their performance has been improved fast in recent years.[1,2] The bulk-heterojunction (BHJ) structure is the most studied structure in which the electron donor polymer and the electron acceptor fullerene are blended as an active layer. The performance improvement of PSCs is mainly attributed to the development of new high performance low-band gap polymers.[3-8] Compared to the donor polymers, few new acceptor materials have been developed. The most widely used are still from fullerene family, like [6,6]-phenyl-C_{61}-butyric-acid-methyl ester ($PC_{61}BM$), [6,6]-phenyl-C_{71}-butyric-acid-methyl ester ($PC_{71}BM$) and Indene-C_{60}-bis-adduct (ICBA).[9] However, the high cost, the lack of absorption in visible spectral region and morphological instability of fullerene derivatives may restrain the commercialization of PSCs in the future.[10]

All-polymer donor-acceptor systems have attracted attentions in recent years because of several potential advantages: 1) Conjugated polymers can be designed to have enhanced absorption coefficients, which can complement the absorption spectra of donor polymers and thus enhance light harvesting by the active layers; 2) The structural variations of polymers enable fine-tuning of energy levels and thereby maximizing performance of PSCs; 3) The film forming properties of polymers can be modified by tuning structures and molecular weights of polymers to control the viscosity of the solution, of importance for large-scale process; 4) Conjugated polymers are potentially stable and cheaper.[11] As a result, the efficiency of all-polymer solar cells has the potential to be further improved.

The first efficient all-polymer bulk-heterojunction PSC was realized in 1995 by Friend and coworkers.[12] After considerable efforts, slow but steady progress has been

[a] *Biomolecular and Organic Electronics, IFM, Linköping University, SE-581 83, Linköping, Sweden. E-mail: oling@ifm.liu.se*
[b] *State Key Laboratory for Mechanical Behavior of Materials, Xi'an Jiaotong University, Xi'an 710049, China*
[c] *State Key Laboratory of Silicon Materials, Department of Materials Science and Engineering, Zhejiang University, Hangzhou 310027, P. R. China*
[d] *Advanced Light Source Laurence Berkeley National Laboratory, Berkeley, California 94720, USA*
[e] *Future Industry Institute, University of South Australia, Mawson Lakes, South Australia 5095, Australia*
[f] *Siyuan Laboratory, Department of Physics, Jinan University, Guangzhou 510632, China*
[g] *Department of Chemistry and Chemical Engineering, Chalmers University of Technology, SE-412 96 Göteborg, Sweden E-mail: ergang@chalmers.se*
† Electronic Supplementary Information (ESI) available. See
DOI: 10.1039/x0xx00000x

achieved. Only a few systems with power conversion efficiency (PCE) above 3% were reported until 2013. Very recently, PCE above 7% has been realized.[11,13-17] However these PCEs are still much lower than those of the high-performance polymer/fullerene systems. All-polymer solar cells generally have lower fill factor (*FF*) and short circuit current density (J_{sc}), which may be related to poor charge generation and collection efficiency.[13,18-20] In order to improve the performance of all-polymer cells, considerable efforts have been devoted to the synthesis of acceptor polymers with high carrier mobility and wider optical absorption range, as well as by optimization of the morphology of active layers. Among various n-type polymers for BHJ solar cells, naphthalene-imide based polymers have favourable characteristics such as high electron mobility and suitable energy level as an acceptor relative to many donor polymers. One of the most popular NDI-based polymers is poly(*N,N*′-bis(2-octyldodecyl)naphthalene-1,4,5,8-bis(dicarboximide)-2,6-diyl-*alt*-2,2′-bithiophene-5,5′-diyl), (**Figure 1**) with a commercial name N2200. It has an electron mobility up to ~0.85 $cm^2 V^{-1}s^{-1}$ and similar energy levels to PCBM.[21] So far the best reported PCEs of all-polymer PSC was obtained by NDI-based polymers as acceptor.[15] Controlling the morphology of the active layers is critical, not only for polymer-fullerene solar cells[22-25] but also for all-polymer solar cells[19,26-28] as it influences the charge generation and transport. For efficient PSCs, the morphology of active layer must simultaneously satisfy many conditions: a) bicontinuous and interpenetrating donor and acceptor (D/A) networks; b) sufficient D/A interfacial area for efficient charge generation; and c) domain sizes on the scale of a few tens of nanometers to match the (expected) exciton diffusion lengths of about 10 nm. Useful strategies to obtain such ideal morphology include processing solvent selection, solvent annealing and thermal annealing. These methods can tune the kinetics and thermodynamics of the formation of BHJ film.[29] Unlike polymer-fullerene systems, the effects of thermal annealing on the performance of all-polymer systems have not yet been well investigated, with only few paper published. [27,30]

Here we selected one of the most efficient all-polymer solar cell systems using poly[2,3-bis(3-octyloxyphenyl)quinoxaline-5,8-diyl-*alt*-thiophene-2,5-diyl] (TQ1)[31] as donor and N2200 as acceptor for the investigation of thermal annealing effect. The TQ1/N2200 blend system was first reported by Mori in 2013,[13] in which a PCE of 4.1 % was obtained in a conventional device structure of ITO/PEDOT:PSS/active layer/Ca/Al. As inverted devices have advantages in stability and lifetime,[22,32,33] in this paper, in addition to the conventional structure, we introduced an inverted structure of ITO/ZnO/active layer/MoO_3/Al. It was found that the device performance was improved up to PCE of 4.4% from 2.4% (as-spun) upon thermal annealing. Reasons for this improvement were investigated through a set of complementary experiments, using spectroscopy, microscopy and device measurements.

2. Results and Discussion

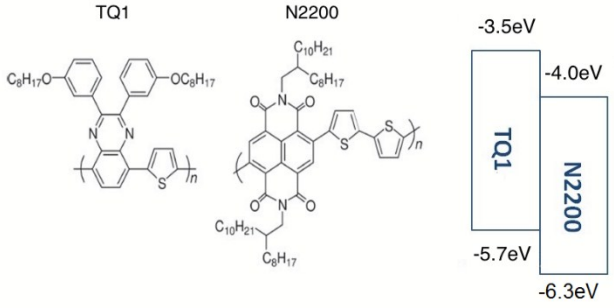

Figure 1. Structures and energy levels alignment of TQ1 and N2200. The M_n of TQ1 and N2200 used in this paper is 69.3 kDa and 43.0 kDa respectively.

Table 1. Photovoltaic data of TQ1-N2200 inverted and conventional devices. Numbers in brackets are average values from 6 devices.

		D/A ratio	J_{sc}(mA cm^{-2})	*FF*	V_{oc}(V)	PCE (%)
Inverted	Annealed	2:1	8.9	0.60	0.82	4.4 (4.0)
	As-spun	2:1	5.8	0.47	0.89	2.4 (2.2)
Conventional	Annealed	2:1	8.9	0.45	0.84	3.4 (3.2)
	As-spun	2:1	5.7	0.45	0.91	2.3 (2.2)

The chemical structures of the two polymers and their energy levels are illustrated in **Figure 1** and the photovoltaic parameters of the all-polymer cells are summarized in Table 1. With TQ1:N2200 blend ratio of 2:1 in inverted structure, the highest PCE of 4.4% (average 4.0%) was obtained after annealing at 120 °C for 10 minutes, which is much higher than the PCE of 2.4% (average 2.2%) in the as-spun devices. Figure 2 shows the current density—voltage (*J-V*) curves and external quantum efficiency (EQE) data of inverted devices before and after annealing. The improved PCE mainly originates from the enhanced J_{sc} (5.8 vs 8.9 mA cm^{-2}) and FF (0.47 vs 0.60) with loss of V_{oc} by 0.07 V (0.89 vs 0.82 V). A similar improvement in PCE has been also observed in devices with a conventional structure (ITO/PEDOT:PSS/active layer/LiF/Al), where the annealed devices exhibit a higher PCE of 3.3% compared to the as-spun devices with a PCE of 2.3%. Compared with reference 13, our conventional devices have a lower FF (0.45 vs 0.55), which might be due to the difference in device structures, where we used LiF and PEDOT: PSS 4083 while they used Ca and PEDOT: PSS PH500 in the reference. It is noted that unlike in the inverted devices, only J_{sc} (5.7 vs 8.9 $mAcm^{-2}$) but not FF was improved in the conventional devices upon annealing. The reason is probably because of different recombination kinetics (possibly more serious surface recombination in conventional devices), which results from different interlayers and different morphology. It should be noted that

the measurements and study in the following part are based on the inverted devices since their performance are higher.[34] Thermal annealing here is proven to be an effective way to enhance the performance for this all-polymer system regardless of the devices structures, as has also been widely observed in polymer/fullerene systems.

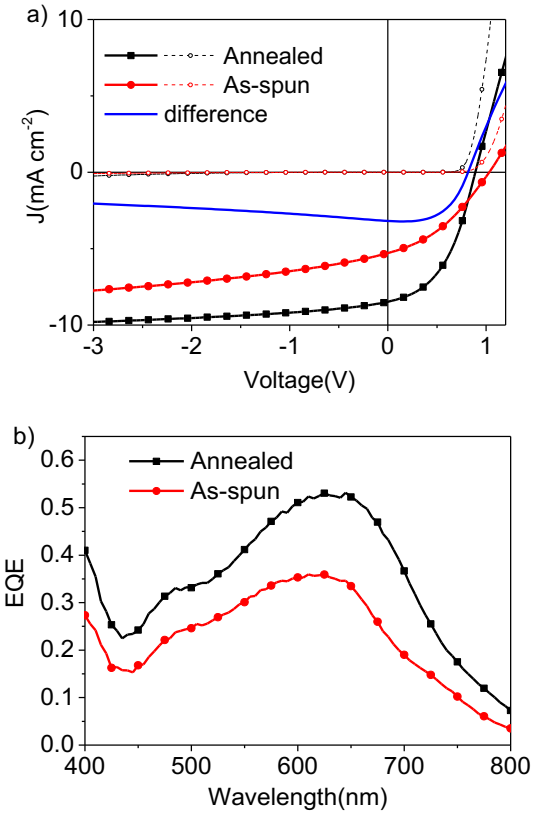

Figure 2. a) *J-V* curves of inverted devices measured under AM 1.5G. The corresponding dark currents (dashed line), photocurrents (solid line) and the difference of the current are also included. b) EQE data of the inverted devices.

It is worth noting that the devices from the all-polymer systems (both inverted and conventional structure) were not stable, and a rapid decay was observed after a period of light illumination even in encapsulated devices. This phenomenon has not been widely reported before. To understand the reasons for the instability, studies of the degradation mechanisms of all-polymer solar cells is ongoing.

To investigate the effect of the annealing on optical, electronic and morphological properties, we carried out a set of experiments including absorption and luminescence spectra, atomic force microscopy (AFM), conductive AFM (C-AFM) and grazing incidence wide-angle x-ray scattering (GIWAXS).

2.1. Absorption

The absorption of the active layer is very important as it limits the maximum obtainable J_{sc}. The absorptance of the neat polymers and active layer blends were characterized with UV–Vis spectroscopy and the extinction coefficient was further determined by ellipsometry, as shown in Figure 3(a) and Figure S1. Two phenomena, a red-shift of the absorption peak and a slight increase in spectrally integrated absorption of the blend films were always observed, as a result of thermal annealing. To investigate the reasons for these phenomena, the absorption characteristics of the two pure polymers were also recorded before and after annealing. The optical absorption of N2200 is virtually unchanged after thermal annealing. This can be attributed to the highly crystalline nature of N2200,[35] where highly ordered structure has already formed in pristine film and therefore optical properties changes induced by crystallinity changes upon thermal annealing is not large enough to be observed. For the TQ1 polymer, an absorption red-shift was observed after thermal annealing. This can be explained by the amorphous (or possibly partial liquid crystalline) nature of TQ1.[36,37] At an annealing temperature higher than the glass transition temperature (T_g) of TQ1 (T_g ~100 °C[38]), the disordered structure that initially forms in pristine film permits chain segments to rearrange and form an ordered structure, which concomitantly leads to an extended π-conjugation length and thus red-shifted absorption spectra.

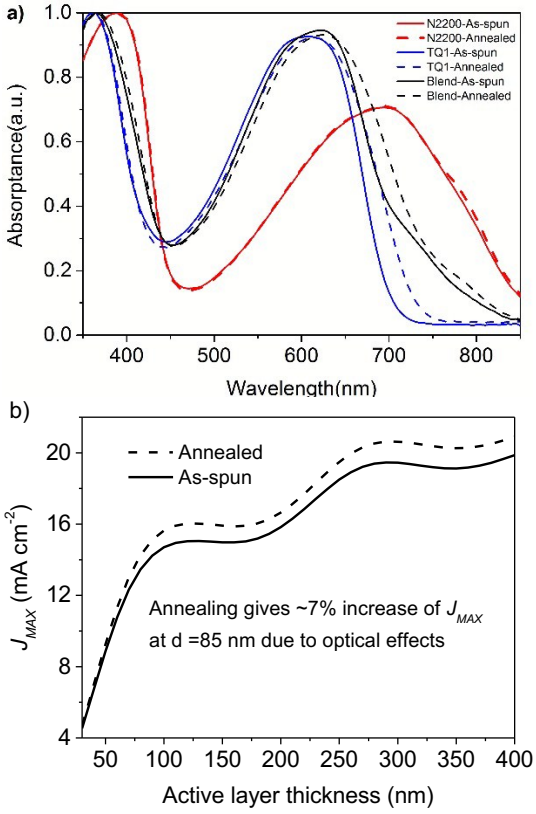

Figure 3. a) Absorptance of the pure polymer and blend. b) The theoretical maximum short-circuit current is calculated through Transfer Matrix Model (TMM). The optimized thickness of active layer is 85 nm at which only 7% increase is obtained by optical change after annealing. The onsets of the absorption are not flat because of the limit of our equipments.

A significant increase in J_{sc} from 5.8 mA cm^{-2} to 8.9 mA cm^{-2} was observed after annealing in inverted devices. The theoretical maximum short-circuit current density J_{max}, varying with the thickness of the films (Figure 3(b)) was calculated, using refractive indexes determined by ellipsometry, through the transfer-matrix optical model (TMM), assuming an internal quantum efficiency of 100%. The J_{max} at the optimal active layer thickness of 85 nm showed only 7% increase, from 13.8 mA cm^{-2} to 14.8 mA cm^{-2}, upon annealing, indicating that the minor increase in optical density cannot account for the observed large increase in J_{sc} upon thermal annealing. It was noted that the experimental J_{sc} value of 8.9 mA cm^{-2} is much lower than the theoretical limit, indicating that there are losses in the processes from photon absorption to carrier extraction at electrodes, which involves charge generation, recombination, transport and extraction. Thus there may still be opportunities to improve the performance of TQ1:N2200 system by tuning the morphology of the active layers.

2.2 Improvement in Charge Carrier Mobility

The red-shifted absorption indicate that the annealing induces more ordered polymer domains, which potentially assists in charge generation and transport. To verify the latter, we first studied the charge transport in the blend using space charge limited conduction (SCLC) measurement. As shown in Figure S2, both hole and electron mobilities increased upon annealing; for electron mobility μ_e, from 1.8×10^{-4} to 6.9×10^{-4} cm^2 V^{-1}s^{-1} and for hole mobility μ_h from 1.6×10^{-5} to 9×10^{-5} cm^2 V^{-1}s^{-1}. This enhancement in charge transport properties can tentatively be explained by the higher order for TQ1 and N2200, and/or better interconnected networks from domain to domain after annealing. To further verify this speculation, the morphology of the blend films was studied with GIWAXS, AFM and conductive-AFM.

2.3 Change of Morphology

GIWAXS was used to investigate the solid-state order of the neat polymer and blend films. The molecular packing orientation can be deduced from the GIWAXS patterns, where the molecular packing out-of-plane appears nominally along the q_z axis and the in-plane ordering along the q_{xy}. The neat films of N2200 exhibit (100), (200) and (300) peaks at 0.26 Å^{-1}, 0.52 Å^{-1} and 0.78 Å^{-1} along q_{xy}, corresponding to a lamellar spacing distance of d_{100} ≈ 24.2 Å, d_{200} ≈ 12.1 Å and d_{300} ≈ 8.1 Å and a (010) peak around 1.6 Å^{-1} along q_z, corresponding to a π-stacking distance d ≈ 3.93 Å (Figure 4 and Figure S3). An additional peak at 0.46 Å^{-1} along q_{xy} can be attributed to the (001) diffraction. This observation coincides quite well with the data reported for N2200 before.[39] The pronounced (010) peak at the out-of-plane direction and absence in the in-plane direction indicates there is a preponderance of face-on orientation with respect to the substrate. It was noted that there is no visible change in the diffraction profiles after annealing, which agrees well with the observation for the identical absorption spectra of N2200 upon annealing. The amorphous TQ1 on the other hand showed no pronounced peaks but some bumps. In the out of plane profile of blend film, we observe a bump from 0.3 Å^{-1} to 0.4 Å^{-1} in the as-spun films but it disappeared after annealing. As this bump was also observed in neat TQ1 films, it can be referred to lamellar stacking (100) response of TQ1. The decrease suggests less lamellar stacking in out-of-plane direction and thus more geometry disorder in this direction. This result seemingly contradicts the increased optical absorption and red-shifted peaks in absorption and emission (discussed later) spectra upon annealing that indicates improved order, but can readily be explained by planarization of single chains of TQ1 rather than interchain stacking. Additionally, although the slight disorder in the lamellar direction is not favorable for better charge transport,[40] it indeed does not result in poorer charge transport in our case. The improved charge transport can also be explained by the planarization of the polymer chain and better interconnected network in the blend.

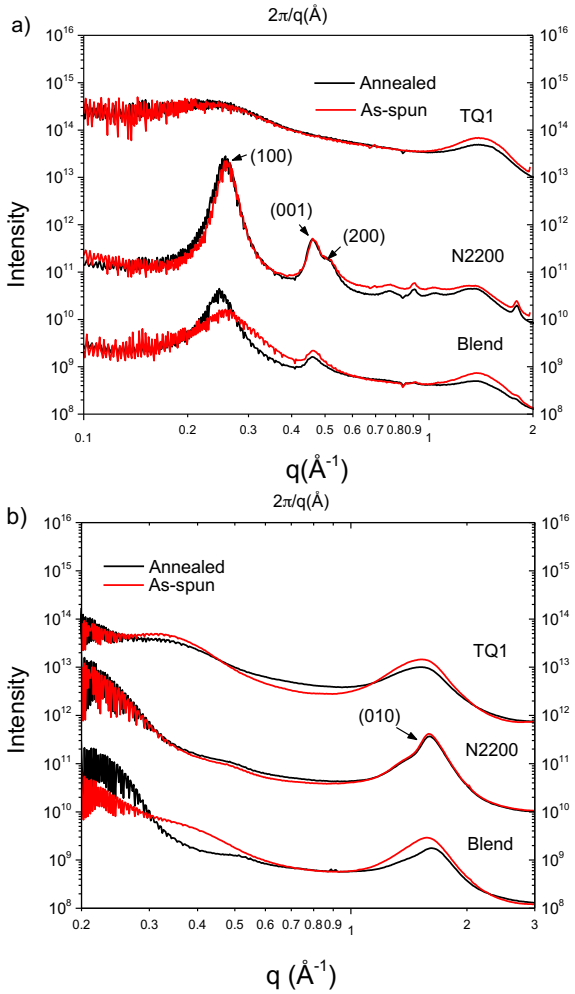

Figure 4. Scattering profiles of a) in-plane and b) out-of-plane for both annealed and as-spun films.

Compared to neat N2200 film, the in-plane lamellar stacking peak (100) of N2200 in the as-spun blend is much weaker, which suggests that the presence of TQ1 inhibits the ordering of N2200. The (100) peak of the annealed blend is higher and narrower than that of the as-spun blend, which indicates that the crystallinity of N2200 in the blend is recovered by annealing treatment. The trend of (010) peaks is identical to the (100) peaks for the blend upon annealing. The quantitatively calculated (010) coherence length (obtained by Scherrer equation[41]) of as-spun and annealed N2200 films is similar. However, the (010) coherence length of the annealed blend is longer than that of the as-spun blend (2.14 nm vs 1.73 nm), suggesting partial restoration of the π- stacking order in N2200.

In agreement with the GIWAXS results, AFM showed a clear nanostructured fibrillar morphology for the N2200 polymer and a more amorphous, bumpy surface for the TQ1 (Figure S4 and S5). From the topography images of the polymer blend (Figure 5 (a), 5(d) and Figure S5), there is no indication about the phase separation. Conversely, the dark current maps (Figure 5(b, c) and (e, f)) obtained by C-AFM measurements, show clear features with distinguishable differences before and after annealing. Comparison of forward and reverse bias images can be used to differentiate between local compositions and provide information about the transport networks. Reference measurements performed on the same sample by oppositely biasing the device showed indeed that complementary regions respond to opposite bias (Figure S7). Under forward bias, holes are injected from the tip, and the current maps show the highest current where holes injection and transport are prevalent (TQ1). Under reverse bias, when lower current values are detected as expected, electrons are injected through the sharp tip, and the current maps show higher current where the sample is N2200-rich. Consistent with the structural properties of the N2200 polymer, these regions appear as fibrillar features in the current maps. In Figure 5, the ITO/ZnO substrate is biased negatively so that the higher current regions (darker areas) represent the TQ1-rich phase and the lower current regions (brighter color) represent the N2200-rich phase.

Thus the current map can provide us with the morphology information in the perpendicular direction with respect to the film plane. Before annealing, the maps showed low current values at almost every position, as an indication of relatively inefficient pathways for holes. However, after annealing, the density of conductive regions increased and definite fiber-like features became visible, which suggests that the annealing can lead to improved transport networks to the bottom electrode and/or enhanced hole injection from the tip.

2.4 Charge generation and recombination

We employed a set of techniques including photoluminescence (PL), electroluminescence (EL) and the light intensity dependence of V_{oc} and J_{sc}, to get insight into how the morphology influences charge generation and recombination.

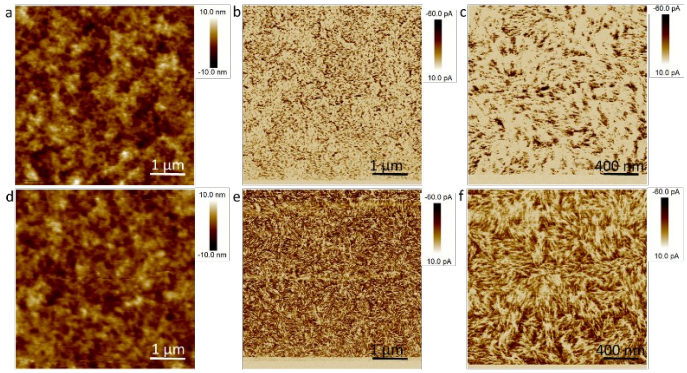

Figure 5. Topography (a, d) and current maps (b, c, e, f) of unannealed (a-c) and annealed (d-f) blends. The current maps are measured under a -2 V bias applied to the ITO/ZnO substrate. The images in c) and f) are enlarged scans taken at different places of the films. In these maps, darker colour correspond to higher current values.

We first discuss the charge generation on the basis of PL experiments, since the charge generation efficiency is correlated to the PL quenching efficiency. The emission from both polymers is significantly quenched in blend films, see Figure S8. A high PL quenching efficiency for TQ1 is observed in the blends, around 99.0% for as-spun and 98.5% for annealed blends, which suggests there are only small domains of TQ1 in the blend. In addition, the good overlap between the PL spectrum of TQ1 and the absorption spectrum of N2200 enhanced the quenching of TQ1 emission by long-range energy transfer.[42] This kind of energy transfer is probably not favourable for charge generation as the excitons in N2200 domains have relative short diffusion length.[43] The PL emission from TQ1 in both pure and blend films showed obvious red-shift from 705 nm to 740 nm in blend (Figure 6(b)) in agreement with the changes in the absorption spectra.

The quenching efficiency for N2200 is relatively lower, 68% for annealed and 45% for as-spun films. Before annealing, a large number of excitons in N2200 phase can decay radiatively to ground state before reaching the heterojunction interfaces to dissociate. After annealing, as the exciton diffusion length in N2200 can increase due to higher crystallinity,[44] the excitons generated in N2200 domains have more chances to reach the interface and then dissociate into free carriers which would help the charge generation and improve J_{sc}.

Light intensity dependencies of the V_{oc} and J_{sc} of the annealed and as-spun devices were measured to further

investigate the recombination. The J_{sc} shows a power law dependence on light intensity.

$$J_{sc} \propto P_{light}^{\alpha}$$

For annealed and as-spun devices, the fitting of data yields α=1.059 and α=1.052, respectively, Figure 7(a), both are quite close to unity within error and it can be taken as an indication of weak bimolecular recombination.

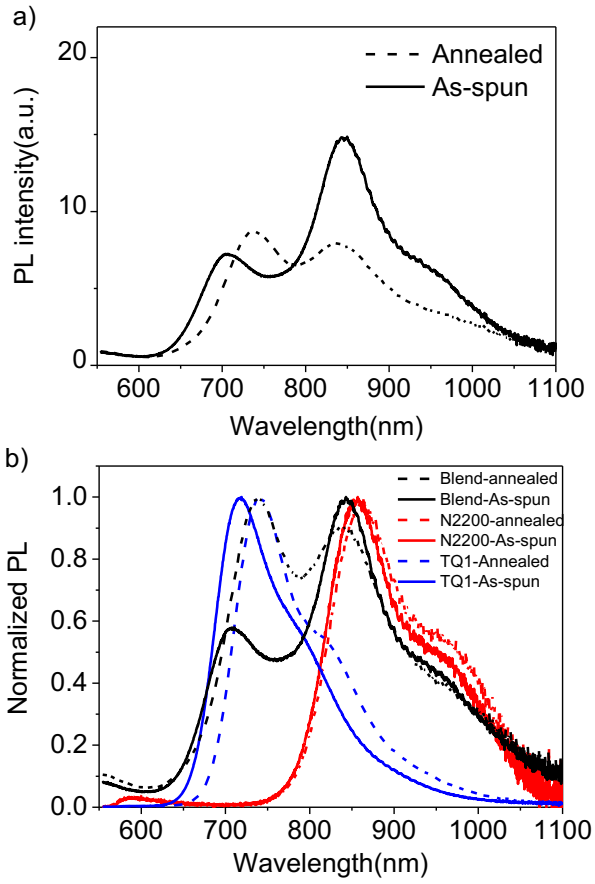

Figure 6. a) PL spectra of the blend film on ZnO pumped by 405nm blue light. b) Normalized PL spectra of pure polymer and blend films.

From *J-V* curves, we can see a field dependence of charge collection both for the annealed and as-spun devices. The difference of the current density under reverse bias between the annealed and as-spun devices decreases with increasing bias, and indicates a higher field dependence of current density in the as-spun devices, implying that recombination is suppressed in the annealed devices. (Figure 2(a)). This can be attributed to the higher dissociation rate due to more charge delocalization along extended conjugation segments of the polymer chains[45,46] and/or less bimolecular recombination due to higher mobility after annealing.

The dependence of V_{oc} on the light intensity is shown in Figure 7(b). The fitted lines show a slope of 1.36 kT/q for the annealed devices and 1.61 kT/q for the as-spun devices, which suggests that the monomolecular recombination (geminate or trap-assisted) is competing with bimolecular recombination in both annealed and as-spun devices.[18,47] The less steep slope after annealing indicates that monomolecular recombination was suppressed. Moreover, here the monomolecular recombination is mainly based on geminate rather than trap-assisted recombination as we discuss in next part.

Though the PL shows emission from both of the two polymers, we can hardly see any emission from CT state

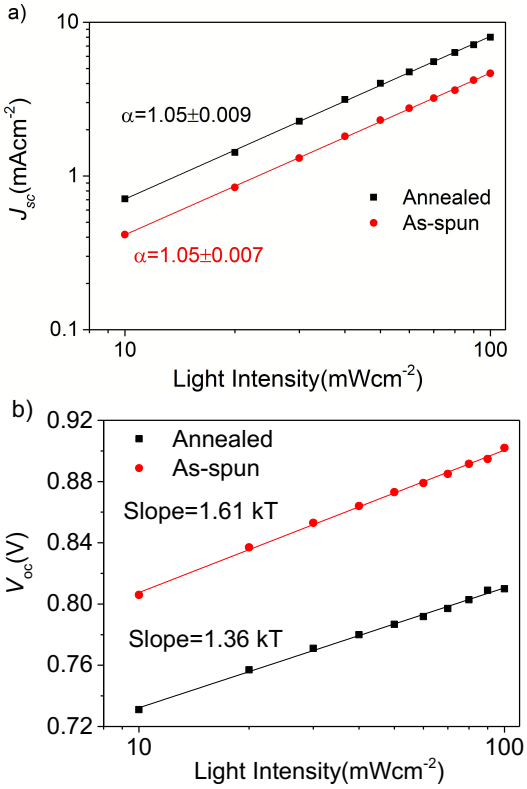

Figure 7. Light intensity dependence of a) J_{sc} and b) V_{oc} based on TQ1:N2200 inverted solar cells. In Fig 7a, the 0.009 and 0.007 are the standard error.

because the PL intensity of the CT recombination might be too weak and there might be overlap between the emission from N2200 and CT state. EL is an easier way to detect the presence as well as energy of the CT states.[48] As electrons and holes are injected into the devices, they must recombine in one way or the other, if not transmitted through the active layer. For the bulk heterojunction, the lowest energetic state that allows for recombination is the CT state. It has been shown that the CT state controls the V_{oc}.[49] It is a rewarding way to find the origins of the altered V_{oc} by CT state emission. We can also get insight of the charge recombination process through EL. Figure 8(a) and 8(b) show the spectra of the blend and neat polymer. New peaks at around 1000 nm, which is absent in either pure TQ1 or N2200 emission, was observed in the blend, and is assigned to the emission from the CT state formed between TQ1 and N2200. For the as-spun blend, emission peaks from TQ1, at around 730 nm, and N2200, at around 860 nm, as well as new emission peaks at around 960 nm can be observed. The annealed devices displayed a lower CT state energy at wavelength about 1010

nm, 0.06 eV lower than that of the as-spun device (~960 nm), which is consistent to the V_{oc} difference of 0.07 V upon annealing. This red-shift of CT emission can be attributed to the lower band gap of TQ1 as observed in absorption and PL after annealing, which results from the planarization of TQ1 polymer backbones.

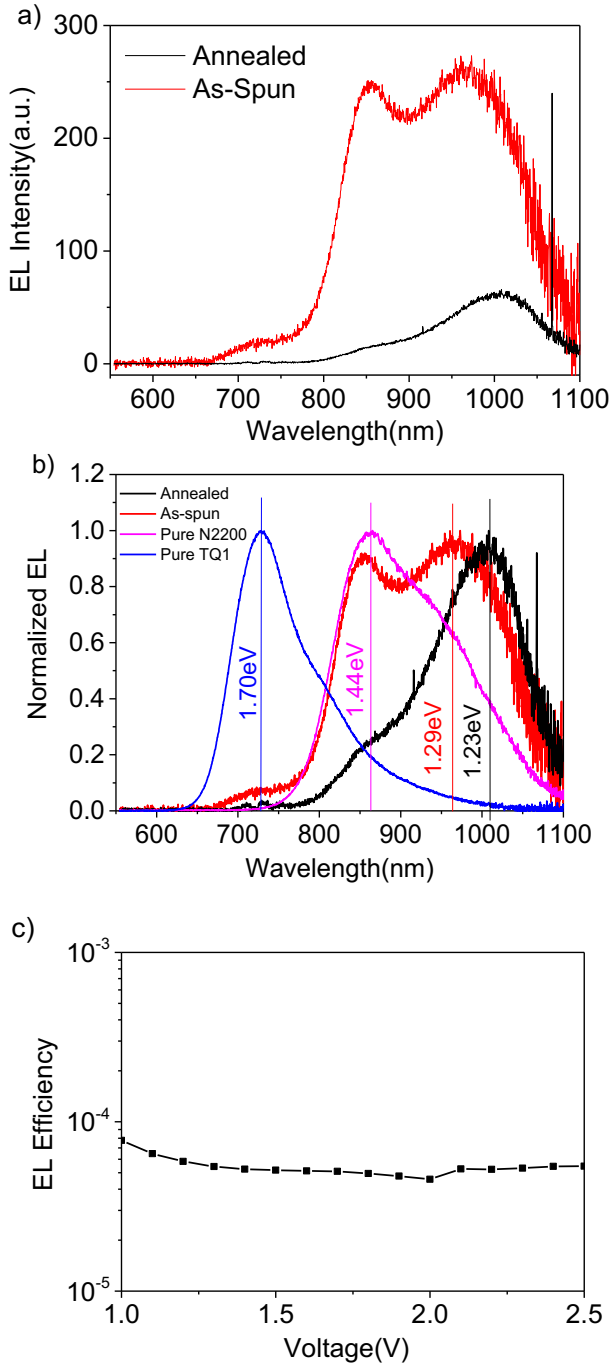

Figure 8. a) EL spectra of blend, annealed and as-spun with the same injection current. b) Normalized EL of pure polymer and blend. c) EL quantum efficiency of the CT state emission as a function of applied voltage for annealed devices.

Apart from the spectral shift, the annealing actually also suppresses the emission from the CT state. The EL was measured under the same injection current but with different applied voltages, 0.9 V for annealed and 1.1 V for as-spun devices. At low applied voltage, recombination through the lowest laying CT state is the more probable way. Generally speaking, upon increasing voltage, more recombination paths through polymer excited states are possible because of increasing concentration of the higher energy states corresponding to the pure polymers. But still, the recombination mainly occurred through lower-energy in CT states, Figure S9. For the as-spun devices under 1.1 V, emission from N2200 at around 860-870 nm is very significant compared to the annealed devices, which can be attributed to inefficient electron transport. Furthermore, we saw a broad N2200 emission spectrum extended to 1000 nm, overlapping with the CT state emission spectrum, which suggests that the CT state in as-spun devices have energy close to that of excitons in N2200. So the emission at 960 nm would be a superposition of the CT state emission on top of N2200 emission. Even so, we can still observe an obvious decrease of the CT state emission after annealing. The reason for the decrease should not attributed to the increase of the non-radiative trap-assisted recombination.[50] This is because the presence of non-radiative trap-assisted recombination should lead to an increase in EL efficiency with increasing applied voltage, which is not observed.[51] The radiative recombination from CT state originates from a bimolecular process, which is quadratically dependent on charge carrier density (and hence on the voltage), while the trap-assisted recombination has linear dependence on charge carrier density. The annealed devices here depict a voltage-independent EL efficiency, Figure 8(c), meaning that the recombination is dominated by bimolecular process. Therefore the explanation for this suppressed emission after annealing is that the formed CT states have more chances to split up into free carriers (because of higher dissociation rate) and then move to the electrodes (because of better charge transport) after annealing.

Conclusion

In conclusion, we investigated thermal annealing effect on high-efficiency TQ1:N2200 all-polymer solar cells. After annealing, devices exhibited higher J_{sc} and *FF*, at an expense of V_{oc}, and finally almost doubling PCE to 4.4%. First of all, the thermal annealing results in significant changes of both electron and hole mobilities. For TQ1, the planarization of polymer backbones induced by annealing not only improved the hole transport ability but also narrowed its band gap and shifted its HOMO level, which leads to lower V_{oc}. Furthermore, through C-AFM measurement, a better interconnected network of TQ1 phase across active layer was observed, verifying that C-AFM is a powerful tool to unveil the morphology of all-polymer systems. Additionally, the use of C-AFM measurement for studying the annealing effect on

all-polymer solar cells, to our knowledge, is not reported previously. Compared to amorphous TQ1, the N2200 is less sensitive to the thermal annealing, but still, the enhanced electron mobility can be attributed to slightly higher crystallinity. From PL, light intensity dependence measurement and EL, charge transport improvement and extended conjugation length after annealing result in more possibility for excitons to dissociate into free charges as well as suppressed recombination, which eventually helps free carrier generation and leads to higher J_{sc} and *FF*. To summarize, the annealing leads to improvement in charge transport, charge generation as well as reduced recombination, and all these effects combined lead to almost a doubled PCE. As to the V_{oc}, the decrease can be explained through the change of CT state energy, as observed in EL. This work demonstrates that, by selecting polymers with appropriate thermal properties, an amorphous polymer, such as TQ1, and a semi-crystalline polymer, like N2200, thermal annealing can promote better interconnected networks without compromising the nanostructure of the blend, which results in significant improvement in photovoltaic performance. The deep understanding of the origin of thermal annealing effect on all-polymer systems is anticipated to boost the development of these emerging system.

Experimental section

Solar Cell Fabrication: solar cells were fabricated using inverted structure glass/ITO/ZnO (25 nm)/active layer (85 nm) /MoO_3 (8.5 nm)/Al (90 nm). The ITO glass was cleaned by detergent and TL-1 treatment (a mixture of water, ammonia (25%), and hydrogen peroxide (28%) (5:1:1 by volume). The cleaned ITO glass was transferred into glove-box filled with N_2, where the ZnO layer and active layer were deposited. ZnO (nanoparticles dissolved in chloroform) was spin-coated on top of the cleaned ITO glass substrates. Then the substrates were heated for 30 min at 150 °C. The active layers were spin-cast from chloroform solutions with a total concentration of 9 mg/mL at spin speed of 3000 rpm for 50 s to achieve a thickness of ~85 nm, and then annealed at 120 °C for 10 minutes. After annealing, MoO_3 and Al layers were deposited by thermal evaporation under a pressure less than 1×10^{-5} mbar. The effective area of the solar cells was ~0.046 cm^2. The J-V curves were measured using a Keithley 2400 Source Meter under AM 1.5G illumination from a solar simulator (Model SS-50A, Photo Emission Tech., Inc.) at 100 mW/cm^2. EQE spectra were measured by a Newport Merlin lock-in amplifier. The chopped monochromatic light was illuminated on the PSCs through the transparent side. Thickness of the active layers were determined using a Dektak surface profiler. The M_n of TQ1 and N2200 is 69.3 kDa and 43.0 kDa, respectively. N2200 was used as purchased from Polyera. TQ1 was synthesised as described in reference 30. MoO_3 was used as purchased from Sigma-Aldrich. ZnO nanoparticles was synthesised as described in reference 32.

GIWAXS: GIWAXS experiment was performed at beamline 7.3.3 of Advanced Light Source (ALS).[52] Samples were prepared using identical blend solutions as those used in devices on a PSS pre-coated Si substrate. The 10 keV X-ray beam was incident at a grazing angle of 0.12°, which maximized the scattering intensity from the samples. The scattered intensity was detected with a Pilatus detector.

AFM and conductive-AFM: AFM and conductive-AFM characterizations were carried out in a Dimension 3100 (Bruker) microscope with a Nanoscope IV controller, equipped with a conductive-AFM module (current sensitivity 1 nA/V). Commercial silicon cantilevers with a nominal spring constant of 40 N/m were used for morphological characterization in tapping mode, while Pt/Cr coated silicon probes with a spring constant of 0.2 N/m were used to perform imaging and measure current maps in contact mode by applying a constant load force of 2-5 nN. For the electrical characterization the tip was always grounded and a variable DC bias was applied to the ITO/ZnO substrate. All the measurements were performed in dark in ambient atmosphere.

PL and EL measurements: an Oriel optical light guide was located close to the biased cell and connected to the entrance slit of the spectrometer. A Newton electron-multiplying CCD (charge-coupled device) Si array detector cooled to -60 °C in conjunction with a Shamrock sr 303i spectrograph from Andor Technology served as the emission-detection system. The system was wavelength-calibrated by an argon lamp to a resolution better than 0.5 nm. The transmission of the entire fibre-monochromator-CDD system was further radiometrically calibrated by an Optronic OL245M standard spectral irradiance lamp. The CCD detector is 'back illuminated', which increases the sensitivity but unfortunately also gives rise to some interference effects at wavelengths between 850 and 1000 nm. Absolute values of the EQE_{EL} spectrum could be obtained by measuring the total number of emitted photons in the 300-1100 nm wavelength range with a homebuilt system using a large-area calibrated Si photodiode from Oriel.

Variable Angle Spectroscopic Ellipsometry was performed on as cast and annealed TQ1:N2200 films spin coated on silicon substrates using an RC2 instrument from J.A. Woolam Co. Inc. The same sample was first measured as cast, then removed and annealed, and then measured again after annealing. The incident angles for measurements was taken in steps of ten degrees from 45 to 75 degrees. The software Complete Ease Co., Inc. was used to model the optical constants with a b-spline model. Also refractive indexes for MoO_3 and ZnO was determined from measurements on silicon substrates using deposition methods identical to those for solar cell fabrication.

Acknowledgement

This work was supported by the Swedish Energy Agency, the Swedish Research council, NSFC (21504006, 21534003), the Knut and Alice Wallenberg Foundation through a Wallenberg scholar grant to Olle Inganäs and also supported by the China Scholarship Council (CSC) and graduate student short-term abroad research project of Jinan University. EW acknowledges the program for the Excellent Doctoral Dissertations of Guangdong Province (ybzzxm201114). FG acknowledges the Open Fund of the State Key Laboratory of Luminescent Materials and Devices (South China University of Technology) (2015-skllmd-02). X-ray data was acquired at beamlines 7.3.3 at the Advanced Light Source, which is supported by the Director, Office of Science, Office of Basic Energy Sciences, of the U.S. Department of Energy under Contract No. DE-AC02-05CH11231.

Notes and References

1. H. Y. Chen, J. H. Hou, S. Q. Zhang, Y. Y. Liang, G. W. Yang, Y. Yang, L. P. Yu, Y. Wu and G. Li, *Nat. Photonics*, 2009, **3**, 649-653.
2. Y. Liu, J. Zhao, Z. Li, C. Mu, W. Ma, H. Hu, K. Jiang, H. Lin, H. Ade and H. Yan, *Nat. Commun.*, 2014, **5**, 5293.
3. T. Y. Chu, J. P. Lu, S. Beaupre, Y. G. Zhang, J. R. Pouliot, S. Wakim, J. Y. Zhou, M. Leclerc, Z. Li, J. F. Ding and Y. Tao, *J. Am. Chem. Soc.*, 2011, **133**, 4250-4253.
4. G. Li, R. Zhu and Y. Yang, *Nat. Photonics*, 2012, **6**, 153-161.
5. J. Nelson, *Materials Today*, 2011, **14**, 462-470.
6. S. C. Price, A. C. Stuart, L. Q. Yang, H. X. Zhou and W. You, *J. Am. Chem. Soc.*, 2011, **133**, 4625-4631.
7. L. P. Yu, Y. Y. Liang, Y. Wu and G. Li, *J. Am. Chem. Soc.*, 2009, **238**, 56-57.
8. E. Wang, W. Mammo and M. R. Andersson, *Adv. Mater.*, 2014, **26**, 1801-1826.
9. Y. He, H.-Y. Chen, J. Hou and Y. Li, *J. Am. Chem. Soc.*, 2010, **132**, 1377-1382.
10. B. A. Collins, J. R. Tumbleston and H. Ade, *J. Phys. Chem. Lett.*, 2011, **2**, 3135-3145.
11. A. Facchetti, *Materials Today*, 2013, **16**, 123-132.
12. J. J. M. Halls, C. A. Walsh, N. C. Greenham, E. A. Marseglia, R. H. Friend, S. C. Moratti and A. B. Holmes, *Nature*, 1995, **376**, 498-500.
13. D. Mori, H. Benten, I. Okada, H. Ohkita and S. Ito, *Adv. Energy Mater.*, 2014, **4**, 1301106.
14. D. Mori, H. Benten, I. Okada, H. Ohkita and S. Ito, *Energy & Environ Sci.*, 2014, **7**, 2939.
15. J. W. Jung, J. W. Jo, C.-C. Chueh, F. Liu, W. H. Jo, T. P. Russell and A. K. Y. Jen, *Adv. Mater.*, 2015, **27**, 3310.
16. Y.-J. Hwang, T. Earmme, B. A. E. Courtright, F. N. Eberle and S. A. Jenekhe, *J. Am. Chem. Soc.*, 2015, **137**, 4424-4434.
17. Y.-J. Hwang, B. A. E. Courtright, A. S. Ferreira, S. H. Tolbert and S. A. Jenekhe, *Adv. Mater.*, 2015, **27**, 4578-4584.
18. M. M. Mandoc, W. Veurman, L. J. A. Koster, B. de Boer and P. W. M. Blom, *Adv. Funct. Mater.*, 2007, **17**, 2167-2173.
19. N. Zhou, H. Lin, S. J. Lou, X. Yu, P. Guo, E. F. Manley, S. Loser, P. Hartnett, H. Huang, M. R. Wasielewski, L. X. Chen, R. P. H. Chang, A. Facchetti and T. J. Marks, *Adv. Energy Mater.*, 2014, **4**, 1300785.
20. Y. Zhou, T. Kurosawa, W. Ma, Y. Guo, L. Fang, K. Vandewal, Y. Diao, C. Wang, Q. Yan, J. Reinspach, J. Mei, A. L. Appleton, G. I. Koleilat, Y. Gao, S. C. Mannsfeld, A. Salleo, H. Ade, D. Zhao and Z. Bao, *Adv. Mater.*, 2014, **26**, 3767-3772.
21. H. Yan, Z. Chen, Y. Zheng, C. Newman, J. R. Quinn, F. Dotz, M. Kastler and A. Facchetti, *Nature*, 2009, **457**, 679-686.
22. M. Campoy-Quiles, T. Ferenczi, T. Agostinelli, P. G. Etchegoin, Y. Kim, T. D. Anthopoulos, P. N. Stavrinou, D. D. C. Bradley and J. Nelson, *Nat. Mater.*, 2008, **7**, 158-164.
23. B. Walker, A. B. Tomayo, X. D. Dang, P. Zalar, J. H. Seo, A. Garcia, M. Tantiwiwat and T. Q. Nguyen, *Adv. Funct. Mater.*, 2009, **19**, 3063-3069.
24. G. J. Zhao, Y. J. He and Y. F. Li, *Adv. Mater.*, 2010, **22**, 4355-4358.
25. X. N. Yang, J. Loos, S. C. Veenstra, W. J. H. Verhees, M. M. Wienk, J. M. Kroon, M. A. J. Michels and R. A. J. Janssen, *Nano Lett.*, 2005, **5**, 579-583.
26. M. Schubert, D. Dolfen, J. Frisch, S. Roland, R. Steyrleuthner, B. Stiller, Z. Chen, U. Scherf, N. Koch, A. Facchetti and D. Neher, *Adv. Energy Mater.*, 2012, **2**, 369-380.
27. D. Mori, H. Benten, J. Kosaka, H. Ohkita, S. Ito and K. Miyake, *Acs Appl. Mater. Interfaces*, 2011, **3**, 2924-2927.
28. W. Yu, D. Yang, X. Zhu, X. Wang, G. Tu, D. Fan, J. Zhang and C. Li, *Acs Appl. Mater. Interfaces*, 2014, **6**, 2350-2355.
29. C. R. McNeill and N. C. Greenham, *Adv. Mater.*, 2009, **21**, 3840-3850.
30. G. Shi, J. Yuan, X. Huang, Y. Lu, Z. Liu, J. Peng, G. Ding, S. Shi, J. Sun, K. Lu, H.-Q. Wang and W. Ma, *J. Phys. Chem. C*, 2015, **119**, 25298-25306.
31. E. Wang, L. Hou, Z. Wang, S. Hellström, F. Zhang, O. Inganäs and M. R. Andersson, *Adv. Mater.*, 2010, **22**, 5240-5244.
32. S. Bai, Y. Z. Jin, X. Y. Liang, Z. Z. Ye, Z. W. Wu, B. Q. Sun, Z. F. Ma, Z. Tang, J. P. Wang, U. Wurfel, F. Gao and F. L. Zhang, *Adv. Energy Mater.*, 2015, **5**, 1401606.
33. S. Bai, S. He, Y. Jin, Z. Wu, Z. Xia, B. Sun, X. Wang, Z. Ye, F. Gao, S. Shao and F. Zhang, *RSC Advances*, 2015, **5**, 8216-8222.
34. Z. Tang, W. Tress, Q. Y. Bao, M. J. Jafari, J. Bergqvist, T. Ederth, M. R. Andersson and O. Inganas, *Adv. Energy Mater.*, 2014, **4**, 1400643.
35. M. Dante, J. Peet and T.-Q. Nguyen, *J. Phys. Chem. C*, 2008, **112**, 7241-7249.
36. E. G. Wang, J. Bergqvist, K. Vandewal, Z. F. Ma, L. T. Hou, A. Lundin, S. Himmelberger, A. Salleo, C. Muller, O. Inganas, F. L. Zhang and M. R. Andersson, *Adv. Energy Mater.*, 2013, **3**, 806-814.
37. J. Bergqvist, C. Lindqvist, O. Backe, Z. Ma, Z. Tang, W. Tress, S. Gustafsson, E. Wang, E. Olsson, M. R. Andersson, O. Inganas and C. Muller, *J. Mater. Chem. A*, 2014, **2**, 6146-

6152.
38. R. Kroon, R. Gehlhaar, T. T. Steckler, P. Henriksson, C. Muller, J. Bergqvist, A. Hadipour, P. Heremans and M. R. Andersson, *Sol. Energ. Mater. Sol. C.*, 2012, **105**, 280-286.
39. J. Rivnay, M. F. Toney, Y. Zheng, I. V. Kauvar, Z. Chen, V. Wagner, A. Facchetti and A. Salleo, *Adv. Mater.*, 2010, **22**, 4359-4363.
40. C. Luo, A. K. K. Kyaw, L. A. Perez, S. Patel, M. Wang, B. Grimm, G. C. Bazan, E. J. Kramer and A. J. Heeger, *Nano Lett.*, 2014, **14**, 2764-2771.
41. D. M. Smilgies, *J. Appl. Crystallogr.*, 2009, **42**, 1030-1034.
42. S. R. Scully, P. B. Armstrong, C. Edder, J. M. J. Frechet and M. D. McGehee, *Adv. Mater.*, 2007, **19**, 2961.
43. Z. Li, J. D. A. Lin, H. Phan, A. Sharenko, C. M. Proctor, P. Zalar, Z. H. Chen, A. Facchetti and T. Q. Nguyen, *Adv. Funct. Mater.*, 2014, **24**, 6989-6998.
44. M. Sim, J. Shin, C. Shim, M. Kim, S. B. Jo, J. H. Kim and K. Cho, *J. Phys. Chem. C*, 2014, **118**, 760-766.
45. S. Albrecht, W. Schindler, J. Kurpiers, J. Kniepert, J. C. Blakesley, I. Dumsch, S. Allard, K. Fostiropoulos, U. Scherf and D. Neher, *J. Phys. Chem. Lett.*, 2012, **3**, 640-645.
46. C. Deibel, T. Strobel and V. Dyakonov, *Phys. Rev. Lett.*, 2009, **103**, 036402.
47. S. R. Cowan, A. Roy and A. J. Heeger, *Phys. Rev. B*, 2010, **82**, 245207.
48. K. Tvingstedt, K. Vandewal, A. Gadisa, F. L. Zhang, J. Manca and O. Inganas, *J. Am. Chem. Soc.*, 2009, **131**, 11819-11824.
49. K. Vandewal, K. Tvingstedt, A. Gadisa, O. Inganas and J. V. Manca, *Nat. Mater.*, 2009, **8**, 904.
50. M. Kuik, L. J. A. Koster, G. A. H. Wetzelaer and P. W. M. Blom, *Phys. Rev. Lett.*, 2011, **107**, 256805.
51. G. A. H. Wetzelaer, M. Kuik, H. T. Nicolai and P. W. M. Blom, *Phys. Rev. B*, 2011, **83**, 165204.
52. H. Alexander, B. Wim, G. James, S. Eric, G. Eliot, K. Rick, M. Alastair, C. Matthew, R. Bruce and P. Howard, *J. Phys.: Conf. Ser.*, 2010, **247**, 012007.